CHEMISTRY OF MATERIALS

Open Access

pubs.acs.org/cm

Article

Growing Gold Nanostars on 3D Hydrogel Surfaces

Gail A. Vinnacombe-Willson,* Clara García-Astrain, Lara Troncoso-Afonso, Marita Wagner, Judith Langer, Patricia González-Callejo, Desirè Di Silvio, and Luis M. Liz-Marzán*

Cite This: *Chem. Mater.* 2024, 36, 5192−5203

Read Online

ACCESS | Metrics & More | Article Recommendations | Supporting Information

ABSTRACT: Nanocomposites comprising hydrogels and plasmonic nanoparticles are attractive materials for tissue engineering, bioimaging, and biosensing. These materials are usually fabricated by adding colloidal nanoparticles to the uncured polymer mixture and thus require time-consuming presynthesis, purification, and ligand-exchange steps. Herein, we introduce approaches for rapid synthesis of gold nanostars (AuNSt) *in situ* on hydrogel substrates, including those with complex three-dimensional (3D) features. These methods enable selective AuNSt growth at the surface of the substrate, and the growth conditions can be tuned to tailor the nanoparticle size and density (coverage). We additionally demonstrate proof-of-concept applications of these nanocomposites for SERS sensing and imaging. High surface coverage with AuNSt enabled 1−2 orders of magnitude higher SERS signals compared to plasmonic hydrogels loaded with premade colloids. Importantly, AuNSt can be prepared without the addition of any potentially cytotoxic surfactants, thereby ensuring a high biocompatibility. Overall, *in situ* growth becomes a versatile and straightforward approach for the fabrication of plasmonic biomaterials.

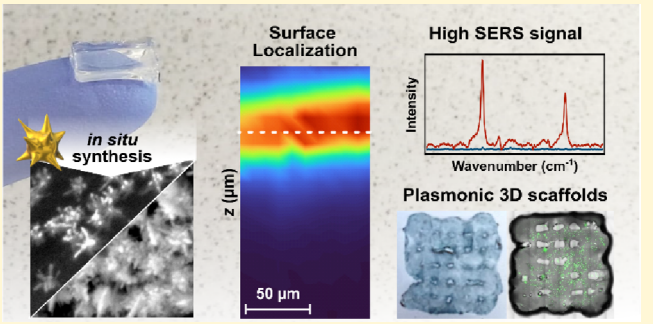

1. INTRODUCTION

Among other fields, plasmonic metal nanoparticles have found broad utility in the biomedical field, as sensors,[1−3] thermoplasmonic therapeutics,[4,5] imaging agents,[6−8] drug carriers,[9−11] and diagnostic tools.[12,13] Many of these applications require the attachment or incorporation of nanostructures on a device or substrate. Both top-down[14,15] and bottom-up[16,17] fabrication methods can be used to create nanoparticle coatings on other materials. Although top-down fabrication provides a high degree of spatial precision, the resulting plasmonic structures are usually of lower quality than those made by bottom-up synthesis, and these techniques may require conditions that are not compatible with all substrate materials, *e.g.*, high vacuum, high temperature.[15,18] Bottom-up synthetic chemistry stands out as one of the most robust and controllable routes for preparing nanostructures with select physical, chemical, and biological properties.[19] For example, it is possible to precisely synthesize a variety of anisotropic colloidal nanoparticles, like stars and rods, with high yields (>90%).[20,21] However, incorporation of colloidal nanoparticles onto substrates or devices usually requires complex multistep processes involving batch synthesis, washing/ligand exchange/surface functionalization, and/or self-assembly.[16,17] Moreover, it is challenging to create plasmonic nanoparticle coatings on substrates with complex 3D features, using either bottom-up or top-down approaches.[19,22,23]

Alternative to conventional top-down and bottom-up fabrication, chemical "*in situ* growth" is an emerging synthetic technique for creating plasmonic substrates whereby nanoparticles are formed directly on the surface of another material via bottom-up chemical reduction of metal salts.[24] In this way, the benefits of a bottom-up chemical-synthetic approach are exploited while avoiding lengthy self-assembly steps. So far, *in situ* growth of plasmonic nanoparticles has been mainly reported on hard substrates, *i.e.*, glass, quartz, indium tin oxide (ITO), and silicon.[25−29] Only a few *in situ* growth procedures for polymers have been reported, with polydimethylsiloxane (PDMS) being the most frequent polymer choice. Overall, both *in situ* seed-mediated and anisotropic nanoparticle growth remain largely unaddressed for materials like soft polymers and hydrogels, which are especially useful for biological applications.[30−32] It has been suggested that, since the particles grow from a substrate support, colloidal stability does not need to be considered and the use of toxic stabilizing surfactants, commonly used in colloidal syntheses, may be circumvented.[24] Additionally, *in situ* growth enables the fabrication of dense nanoparticle coatings on substrates with curved or complex 3D features.[29,33] However, *in situ* growth on 3D substrates has mainly been demonstrated in microfluidic

Received: February 28, 2024
Revised: April 11, 2024
Accepted: April 12, 2024
Published: May 6, 2024

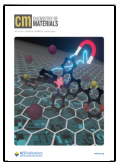

channels, and there is a need for *in situ* growth strategies that can be readily translated to substrates with different and complex constructions.

Integration of hydrogels with plasmonic nanoparticles is of high interest toward creating "nanocomposites" for tissue engineering, photothermal platforms, and surface-enhanced Raman scattering (SERS) bioimaging and sensing.[34−36] Common hydrogels used for biological applications are based on polymers like collagen, gelatin, alginate, and hyaluronic acid.[37−41] Hydrogels composed of gelatin methacryloyl (GelMA) see widespread use in tissue and tumor mimics,[42,43] cell culture substrates or scaffolds,[44,45] biosensors,[46] and therapeutic platforms,[47] due to their excellent biocompatibility (the base component, gelatin, is a natural biopolymer) and the high degree of tunability of GelMA's physical properties.[38] The main approaches for the fabrication of hydrogel nanocomposites include: (i) mixing colloidal nanoparticles with the uncured hydrogel polymer[34,35,48,49] and (ii) nanoparticle growth induced by ultraviolet (UV) light irradiation of the metal precursor.[50−52] With either of these strategies, nanoparticles are introduced throughout the entire gel, which may undesirably alter the polymer's physical and chemical properties.[49,53,54] Regarding sensing applications, additional drawbacks may include a reduced visible−NIR transparency, as well as hindered diffusion of large/less hydrophilic analytes to particle-containing sites,[49] which are important factors for applications where molecules, tissues,[55] or seeded cells are to be analyzed by SERS (*i.e.*, in tissue/tumor models, drug delivery platforms, films/wearable sensors, *etc.*). Electrochemical growth is another popular method for growing metal nanoparticles on semiconductor and conductive polymer surfaces specifically.[56−59] However, controlling the morphology and yield of anisotropic particles with electrochemical growth is still challenging.[56,59]

We hypothesized that *in situ* growth can be used to create coatings of anisotropic gold nanoparticles selectively on the surface of soft materials like hydrogel substrates, including those with complex geometries. Specifically, we demonstrate the *in situ* fabrication of gold nanostars (AuNSt) on bulk GelMA discs (1 cm diameter) and on 3D-printed scaffolds. We targeted AuNSt because they exhibit multiple sharp features hosting hotspots, which are efficient photothermal heaters and enable significant enhancement of Raman signals for biosensing and bioimaging applications.[7,60−62] We tested various routes based on both seed-mediated and seedless bottom-up syntheses, which may offer different advantages depending on the target application. We show that the *in situ* approach is highly tunable, allowing modulation of the density and size of the obtained nanostructures, through variation of the growth conditions. Lastly, we evaluate the performance of various − labeled and label-free − nanocomposites for SERS applications in chemical and biological sensing and SERS imaging.

2. EXPERIMENTAL SECTION

2.1. Materials. Gelatin from porcine skin (gel strength 300, type A), 2-hydroxy-4′-(2-hydroxyethoxy)2-methylpropiophenone (irgacure, 98%), methacrylic anhydride (with 2,000 ppm topanol A as inhibitor, ≥ 94%), and collagenase type II (from collagen type A) were all purchased from Merck. Collagen type I (rat tail high concentration) and fibronectin (human, natural) were purchased from Corning. Analytical grade reagents, silver nitrate ($AgNO_3$; ≥99.9%), $HAuCl_4{\cdot}3H_2O$ (≥99.9%), L-ascorbic acid (99%), *N*-dodecyl-*N*,*N*-dimethyl-3-ammonio-1-propanesulfonate (laurylsulfobetaine (LSB); 99%), hydrochloric acid (HCl; 37%), sodium citrate tribasic dihydrate (citrate; ≥ 98%), Triton X-100 (TX; laboratory grade), 4-mercaptobenzoic acid (4-MBA; 99%), *O*-[2-(3-mercaptopropionylamino)ethyl]-*O*′-methylpolyethylene glycol (PEG-SH 5,000 MW), and 200 proof ethanol (≥99.8%), were obtained from Merck. MDA-MB-231 cells were purchased from the American Type Culture Collection (ATCC, HTB-26). Dulbecco's modified Eagle's medium (DMEM), fetal bovine serum (FBS), and penicillin-streptomycin (PS) were purchased from Invitrogen. FBS and PS were used at 10% and 1%, respectively, to prepare complete DMEM (cDMEM). All cultures were grown in standard conditions at 37 °C with 5% CO_2.

2.2. GelMA Synthesis. Gelatin methacryloyl (GelMA) was prepared by dissolving 5 g of gelatin in 100 mL of 1× phosphate buffered saline (PBS) solution at 50 °C, adapted from previous works.[63−65] After gelatin was fully dissolved, 4 mL of maleic anhydride was added quickly under stirring (1000 rpm). The solution was left to stir at 50 °C for 4 h, then purified by dialysis against water for 5 days (45 °C, 400 rpm stirring), replacing water twice per day. The solution was then isolated by freeze-drying. Hydrogels were made by preparing a 10% w/w aqueous solution of GelMA with 0.5% w/w photoinitiator irgacure at 70 °C. Once fully dissolved, ∼200 μL of the solution was added into a square or circular well with a diameter of ∼1 cm and then cured with a UV lamp (Vilber Lourmat, VL-230, 30 W, 365 nm) for 30 min.

2.3. Gold Nanoparticle Synthesis. All glassware, lids, and magnetic stir bars used for all syntheses were cleaned thoroughly with *aqua regia* (3:1 concentrated HCl to HNO_3 (68%, CAS: 7697-37-2)) and rinsed thoroughly with Milli-Q water three times before use. *Warning: Aqua regia* is extremely corrosive and causes severe burns. Care is needed for its preparation and usage.

2.3.1. Colloidal Synthesis. Gold seeds were synthesized following an established protocol.[21] An aqueous 1% sodium citrate solution (15 mL) was added to an aqueous solution of gently boiling 1 mM $HAuCl_4$ (100 mL) under vigorous stirring (>1000 rpm) in a 200 mL Erlenmeyer flask. After a few seconds, the stirring was stopped, the hot plate was turned off, and the solution was left undisturbed for 15 min. The final solution was cooled to room temperature and stored at 4 °C.

Citrate-capped AuNSt were prepared following a previously reported method.[21] In a typical synthesis, 5 mL of Milli-Q water was combined with 5 μL of 1 M HCl and 25 μL of 50 mM $HAuCl_4$ and mixed by hand. Then, 100 μL of seeds ($Abs_{400\ nm}$ = 1.2) was added rapidly to the solution. This was immediately followed by the simultaneous rapid addition of 30 μL of 10 mM $AgNO_3$ and 25 μL of 100 mM ascorbic acid, under vigorous magnetic stirring (>1000 rpm). Functionalization of the colloidal stars with 4-MBA was performed following a previously reported method:[66] 20 μL of 0.1 mM PEG-SH (5,000 MW) was added for every 10 mL of AuNSt solution under stirring (1000 rpm). The stars were centrifuged at 7,500 rpm for 10 min, followed by resuspension in Milli-Q water. Typical zeta-potential values were between −23 and −30 mV at pH 5−5.5.

2.3.2. In Situ Seed-Mediated Synthesis. The substrates were placed directly in the seed solution and the tube was shaken by hand occasionally to ensure that the entire sample could be covered with seeds. After 15 min, the substrate was removed from the seed solution and rinsed with Milli-Q water. For LSB synthesis, a growth solution containing 4 mL of 100 mM LSB, 60 μL of 50 mM $HAuCl_4$, 60 μL of 10 mM $AgNO_3$, and 40 μL of 1 M HCl was prepared based on a reported method.[29] Then, 200 μL of 100 mM ascorbic acid was quickly added with stirring (∼1000 rpm). When the solution became clear (∼2 s), the seeded hydrogel was added. For the synthesis with TX, the same stepwise process was followed, but using 5 mL of 100 mM TX, 50 μL of 50 mM $HAuCl_4$, 50 μL of 10 mM $AgNO_3$, 150 μL of 1 M HCl, and 160 μL of 100 mM ascorbic acid, a modified recipe based on previous work.[33,67,68] Additionally, because a higher quantity of HCl was used in the TX synthesis, the solution became clear within ∼7 s (instead of ∼2 s). The substrates were recollected from the growth solution and rinsed with Milli-Q water after 10 min.

https://doi.org/10.1021/acs.chemmater.4c00564
Chem. Mater. 2024, 36, 5192−5203

2.3.3. Seedless In Situ Synthesis. In the single-step synthesis, GelMA substrates were added directly to a growth solution containing 4 mL of Milli-Q water, 60 μL of 50 mM $HAuCl_4$, and 60 μL of 10 mM $AgNO_3$ for ∼30 s. Then, 100 μL of 100 mM ascorbic acid was added quickly under mild stirring (∼500 rpm). The solution should change color to a purple-pink color after ∼10 s. After 5 min, the substrate was removed and rinsed with water. The preloaded synthesis was carried out by incubating the substrates in 2.5 to 50 mM ascorbic acid aqueous solutions from 5 min to 3 h, as indicated (the selected standard condition is 25 mM ascorbic acid for 30 min). Then, the substrates were removed from the solution and rinsed with Milli-Q water. The substrates were then incubated in a growth solution containing 4 mL of water, 60 μL of 50 mM $HAuCl_4$, and 60 μL of 10 mM $AgNO_3$ with occasional stirring by hand. After 5 min, the substrate was removed from the solution and rinsed with water.

2.4. 3D Printing GelMA Scaffolds and Cell Seeding. A multiheaded 3D Discovery bioprinter (RegenHU, Switzerland) was used for extrusion-based printing of the hydrogel scaffolds. A pressure-driven dispenser was employed to extrude the material by using a conical plastic needle with an internal diameter of 0.41 mm. The ink was kept at 10 °C by using a cartridge cooler. The G-code for square scaffolds was produced by using BIOCAD software (RegenHU, Switzerland) with 1.5 mm spacing between fibers. The scaffolds were printed at 10 mm s^{-1} flow rate and 0.180 MPa. After each layer was deposited, GelMA was cross-linked *in situ* using a light curing kit cartridge at 365 nm (output power of 500 mW). Finally, the printed scaffolds were irradiated with a UV lamp for 1.5 min. The scaffolds were functionalized with a fibronectin/collagen coating: 2.5 μL of 1 mg/mL fibronectin and 5.7 μL of 8.24 mg/mL collagen were added to 969.3 μL of cell medium (DMEM) and incubated with the sample at 37 °C for 1 h. The substrates were then incubated with 500 μL of MDA-MB-231 cell suspension (1×10^6 cells/mL) at 37 °C for 24 h. The cell viability was evaluated using standard calcein-AM/propidium iodide live/dead staining.

2.5. Characterization. Spectroscopic and rheological characterizations of hydrogels were performed using an Agilent 8453 UV−visible−NIR photodiode array spectrophotometer and an MCR 302 rheometer (Anton Paar, Spain), respectively. The GelMA solid was characterized by ^{1}H NMR (500 MHz, D_2O), and the chemical shift scale was adjusted to the solvent residual signal D_2O δ (1H) = 4.79 ppm (full details are provided in the Supporting Information).

Transmission electron microscopy (TEM) images were collected with a JEOL JEM-1400PLUS transmission electron microscope operating at 120 kV. The particles grown on hydrogels were collected for TEM characterization by incubating the substrates in a 1 mL solution of collagenase at 1 mg/mL (∼200 U/mL) in PBS and incubating at 37 °C for 2 days until GelMA was dissolved. The solution was washed by centrifugation twice (15 min, 7.5 krpm), resuspended in water, and then drop-cast onto a TEM grid. Zeta potential measurements were obtained for 4-MBA capped AuNSt, by using a Malvern Zetasizer 3000 HS particle size analyzer (Malvern Instruments, U.K.). The colloidal nanoparticle solutions were set to an extinction of 0.3 at 400 nm.

Scanning electron microscopy (SEM) images were acquired on a Quanta-FEG 250 ESEM instrument (Field Electron and Ion Company, FEI; Hillsboro, Oregon, United States). Hydrated gels were measured in environmental mode, at 10−20 kV, spot 3−4, 655 Pa, with a live fiber detector (LFD). The cross-sections of the gels were prepared by the freeze-fracture method, dried, and imaged under low-vacuum conditions. The images of the scaffold were obtained with a JSM-IT800HL from JEOL (Tokyo, Japan) equipped with a top-view backscatter electron detector (BSE detector, scintillator-photomultiplier detector design) using 3−5 kV, under a high vacuum.

Raman spectra comparing the SERS intensities of 4-MBA were acquired using an inVia Renishaw Raman microscope. 2D *z*-maps of the substrates were performed with a confocal Raman microscope (Alpha300 R − Confocal Raman Imaging Microscope, Witec GmbH, Germany). Full measurement parameters are given in the Supporting Information.

XPS experiments were performed in a Versaprobe III Physical Electronics (ULVAC) spectrometer with a monochromatic X-ray source (aluminum Kα line of 1487 eV), calibrated using the $3d_{5/2}$ line of Ag at 368.26 eV (additional details are provided in the Supporting Information).

Confocal images were recorded in a Zeiss LSM 880 confocal laser scanning microscope, equipped with 405 nm (blue fluorophore excitation), 488 nm (green fluorophore excitation), and 633 nm (far red fluorophore excitation) lasers and Plan-Apochromat 10× (0.45 NA) and Plan-Apochromat 20× (0.8 NA) objectives. The z-stacks (*ca.* 50 μm thick) of the 3D scaffolds with MDA-MB-231 cells were obtained and a postimaging maximum intensity projection (MIP) filter was applied.

3. RESULTS AND DISCUSSION

Taking inspiration from colloidal methods, we initially approached the fabrication of AuNSt surface coatings using a hybrid strategy combining colloidal and *in situ* growth. This so-called seed-mediated growth involves nanoparticle nucleation and growth steps being performed sequentially in separate reaction steps and is one of the most established bottom-up synthetic methods for AuNSt.[21,33,67−70] Therefore, our first strategy involved the attachment of colloidal seeds to the precured gel, followed by *in situ* overgrowth of branches from the immobilized seeds. Established colloidal AuNSt protocols employing the shape-directing surfactants laurylsulfobetaine (LSB) and Triton X-100 (TX) were adapted for *in situ* overgrowth on GelMA hydrogels, according to the procedure schematically shown in Figure 1A.[33,67,68] 10% w/w GelMA hydrogels were prepared as described in the Experimental Section. Then, the GelMA substrates were incubated in a dispersion of presynthesized ∼13 nm citrate capped nanospheres (prepared by the Turkevich-Frens method, Figure S1),[71,72] leading to uniform adsorption, as confirmed by SEM (Figure S2). Next, the mild reducing agent ascorbic acid was added to a growth solution containing $HAuCl_4$ and other shape-directing reagents (LSB, TX, $AgNO_3$, and HCl; see Experimental Section), and the seeded substrate was introduced into this growth solution immediately. The resulting structures were analyzed by both TEM and SEM, as illustrated in Figure 1B−F (low-magnification SEM images and size distributions are provided in Figures S3−S5). The resulting composite hydrogels showed a dark blue color (Figure 1A).

We aimed at promoting AuNSt growth specifically on the substrate, meaning that secondary nucleation of colloids in the growth solution, which directly competes with on-substrate growth by the consumption of reagents, should be prevented by tuning the reaction conditions. In the case of LSB-capped AuNSt (AuNSt@LSB), the appropriate reaction conditions yielding minimum secondary nucleation were selected, based on prior reports for *in situ* preparation of AuNSt@LSB on PDMS,[31,32] silane-functionalized glass, and ITO substrates.[29,33] Secondary nucleation was prevented by slowing the reaction through addition of HCl, thereby decreasing the concentration of ascorbate anions responsible for the reduction of Au^{3+} into Au^+. Ascorbic acid is also used as a mild reducing agent in the TX-capped AuNSt (AuNSt@TX) synthesis, so a similar strategy may be used to adapt the colloidal protocol *in situ*. The synthesis was optimized by varying the concentration of HCl, as described in Figure S6. Both AuNSt@LSB and AuNSt@TX could be dispersed for TEM characterization by dissolving GelMA in a collagenase solution. The recovered LSB- and TX-stabilized AuNSt had average tip-to-tip diameters

https://doi.org/10.1021/acs.chemmater.4c00564
Chem. Mater. 2024, 36, 5192−5203

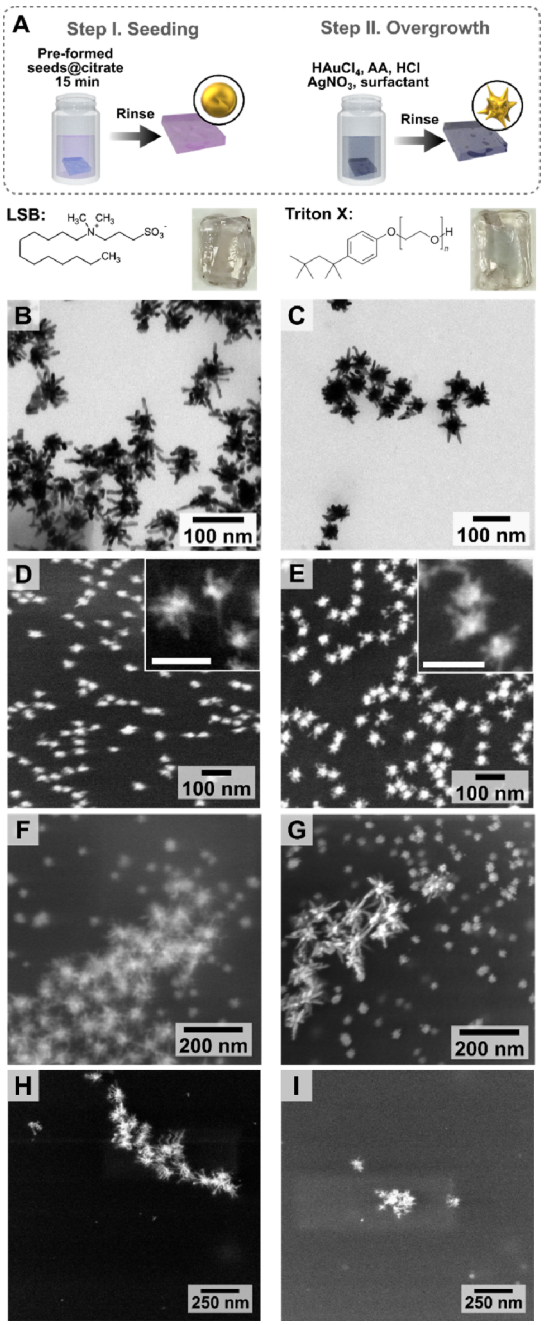

Figure 1. (A) Schematic illustration of the growth of gold nanostars (AuNSt) from colloidal Au@citrate seeds in the presence of laurylsulfobetaine (LSB) and triton X-100 (TX) as surfactants. The chemical structure of the ligands and digital photographs of the final substrates are shown below the scheme. TEM images of AuNSt@LSB (B) and AuNSt@TX (C), collected after dissolving GelMA. SEM images showing AuNSt at the hydrogel surface for AuNSt@LSB (D, F) and AuNSt@TX (E, G). *Scale bars of insets:* 100 nm. Additional SEM images are provided in Figures S2−S4, and size distributions are plotted in Figure S5. SEM images of the substrate after incubation in a growth solution containing LSB (H) and TX (I), with no seeding step (control experiments).

of 51 ± 24 and 57 ± 15 nm and core diameters of 20 ± 15 and 34 ± 4 nm, respectively (n = 150; Figure S5). TEM analysis confirmed that both products exhibited branched morphologies (Figure 1B,C) and the presence of AuNSt coatings at the surface of the hydrogel was confirmed by SEM (Figure 1D,E). Ultimately, the morphology and branching of AuNSt@TX were similar to those of AuNSt@LSB (Figure 1C,E,G).

Unexpectedly, second populations of much larger AuNSt were consistently obtained from seeded-growth syntheses using both TX and LSB (Figure 1F,G). Low-magnification SEM images showed that the distributions of seeds (prior to seeded growth) and small AuNSt were alike (Figures S2−S4). We therefore hypothesized that ∼50−60 nm stars do result from seed-mediated growth, whereas larger AuNSt could stem from either: (i) secondary nucleation in solution, then deposition of the colloidal particles on the substrate or (ii) spontaneous nucleation and growth of nanostars directly on the gel (not from adsorbed seeds). Control experiments comprising only the second synthetic step (no seeding) yielded products consistent with the morphology of the larger AuNSt, thereby supporting the latter hypothesis (ii) (Figure 1H,I). Observation of negligible secondary nucleation in solution − due to HCl addition − also indicates that the large AuNSt are indeed produced from direct nucleation on GelMA.

Ideally, the realization of a fully *in situ* growth method without the need for any colloidal presynthesis steps would further simplify and reduce the preparation time for the nanocomposites. Therefore, we optimized AuNSt growth directly from the gel without any surfactants or seeds, following the procedure sketched in Figure 2A ("single-step" seedless *in situ* growth). When the cured hydrogels (prepared as described in the Experimental Section) were incubated in an aqueous solution containing $HAuCl_4$, $AgNO_3$, and ascorbic acid, products with branched morphologies were also obtained (41 ± 18 nm tip-to-tip and 20 ± 7 nm core diameter, n = 150, Figure 2B), which could be extracted and characterized by TEM (Figure 2B, *inset*). However, unlike the seeded synthesis in the presence of LSB and TX, significant secondary nucleation occurred under these growth conditions. UV−visible spectroscopy and TEM characterization showed that the products found in the growth solution (collected immediately at the time when substrate growth was completed) had morphologies different from those found on the gel (Figures 2C,D and S7). The observation that the particles present in the growth solution and those on the substrate were distinct in both size distribution and shape supports the idea that particles on the substrate did not arise from the deposition of colloidal particles. Incubation of the substrate with premade surfactant-free AuNSt@citrate, even overnight, did not result in deposited particles on the gel, further supporting this conclusion (Figure S8). Altogether, these data indicate that nanostars did grow directly on the gel surface, as desired.

Even though single-step synthesis did successfully produce nanostar coatings, we decided that both coverage and yield of AuNSt (typically ∼60−70% yield) could be improved. Therefore, a different growth strategy was pursued to further reduce undesired secondary nucleation and favor AuNSt growth *in situ*. In this case, we attempted to prevent secondary nucleation by confining the reducing agent to the substrate (ascorbic acid "pre-loaded" seedless *in situ* growth), following the process sketched in Figure 2E. The cured hydrogels were first incubated in ascorbic acid solution at the chosen concentration (between 2.5 and 50 mM) for a certain period (5 min to 3 h), then the sample was rinsed with Milli-Q water to prevent excess ascorbic acid from causing secondary nucleation in solution. The substrate was finally immersed in a growth solution containing $HAuCl_4$ and $AgNO_3$, under

https://doi.org/10.1021/acs.chemmater.4c00564
Chem. Mater. 2024, 36, 5192−5203

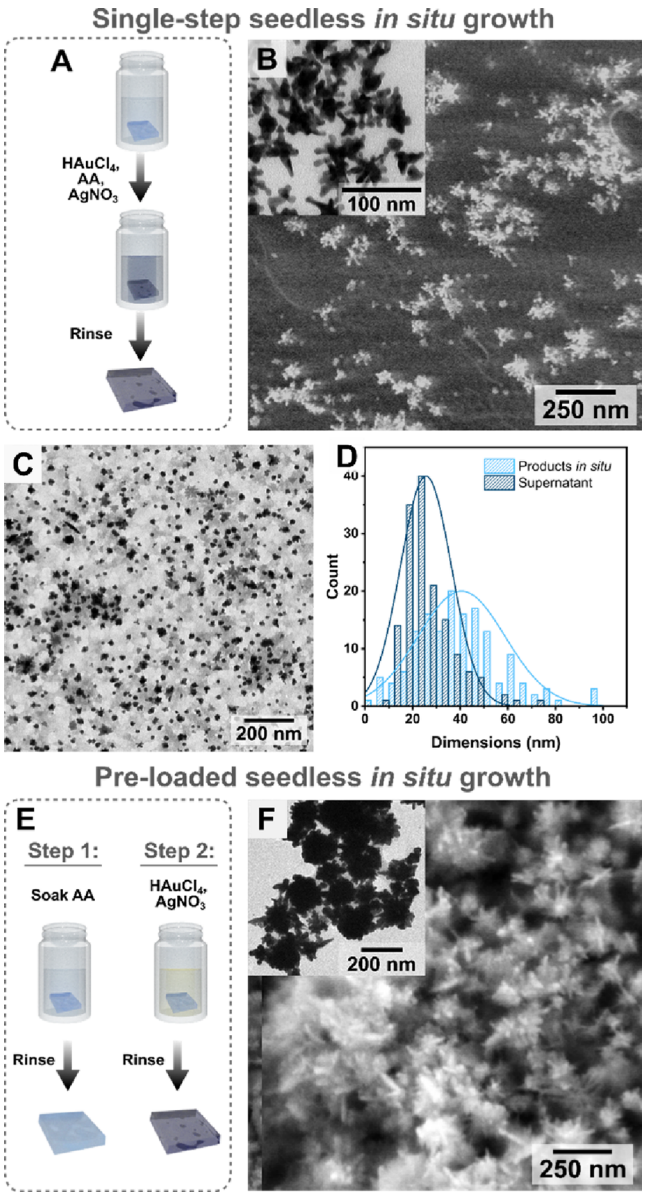

Figure 2. (A) Schematic view of the process for *in situ* single-step growth for gold nanostars on gelatin methacryloyl. (B) SEM image of the products on the gel surface, and (*inset*) TEM image of particles collected from the dissolved gel. (C) TEM image of the particles formed in the growth solution (as a result of secondary nucleation, not grown on the substrate; Ø = 26 ± 11 nm for the supernatant and Ø tip-to-tip = 41 ± 18 nm for *in situ* products, respectively; n = 150). (D) Size distribution of the products in the growth solution vs those formed on the substrate. (E) Scheme describing the synthesis of gold nanostars in a preloaded fashion, where nanoparticles form specifically on the substrate, rather than both on the substrate and in solution. (F) SEM image of nanostars prepared using the preloaded approach, and (*inset*) TEM image of particles collected after dissolving the gel. Additional SEM images are provided in Figures S9, S10, and S12, and size distributions are plotted in Figure S11.

magnetic stirring (see the Experimental Section for details). Any secondary nucleation in the supernatant was monitored by UV−visible spectroscopy (Figure S11), and the products were evaluated with SEM (Figure S12). Dense coatings of highly branched structures were obtained at incubation times of 30 min in 25 mM ascorbic acid (Figures 2F and S10). These particles were larger (~100 nm tip-to-tip with ~80 nm core size, n = 150, Figure S11C) than those formed by the single-step method, in which ascorbic acid was directly added to the growth solution, consistent with an increased yield of *in situ* gold reduction. It should be noted that large AuNSt with no capping ligands are challenging to prepare in colloidal suspension due to their tendency to aggregate or reshape but are advantageous for SERS and other applications due to their high scattering efficiency, robust local electromagnetic fields, higher degree of branching, and easier analyte adsorption, thereby highlighting yet another advantage of the *in situ* growth method.[1,62,73,74]

Going forward, we interrogated the general mechanism behind direct *in situ* growth and considered that it may be related to the coordination of Au^{3+} to the native chemical functionalities of GelMA, specifically related to the presence of peptide bonds, which was studied by Raman scattering and X-ray photoelectron spectroscopy (XPS). Gelatin comprises various amino acids, thus containing secondary amides and carbonyl groups from peptide bonds and amino acid residues (*e.g.,* proline contributes pyrrolidine groups) (Figure 3A). Different quantities of primary amines, also capable of coordinating to Au^{3+}, are present depending on the methacrylation degree, which was evaluated as ~80% for a typical batch prepared as described above (see also the Materials and Methods section in the Experimental Section; ^{1}H-NMR characterization is shown in Figure S13).

When GelMA was incubated in an aqueous solution of $HAuCl_4$, the substrate changed from clear to yellow within a few minutes, then to orange after ~24 h, and to deep red after ~48 h (Figure S14). The initial color change from clear to yellow/orange is likely due to the coordination of Au^{3+} to GelMA *via* nitrogen- and oxygen-containing functional groups (secondary amides and a small population of primary amines − considering that only ~20% of lysine residues are non-methacrylated).[37] Raman scattering measurements showed the disappearance of two bands following incubation with $HAuCl_4$ for 24 h: the Amide I band at 1603 cm^{-1} and the weak C−H_2 twisting band (possibly corresponding to the pyrrolidine ring) at 1172 cm^{-1} (Figure 3B,C). Furthermore, the amide I and amide III bands at 1666 and 1235 cm^{-1}, respectively, shifted toward lower frequencies, consistent with metal ion coordination to amide regions (Figure S14, and Raman peak assignments are given in Table S2). The final color change from orange to deep red suggests complete reduction into Au^0, in the presence of GelMA (without any added reducing agents). Therefore, GelMA itself acts as a reducing agent in the synthesis. Indeed, XPS and SEM characterization confirmed both the presence of Au^0 and the formation of nanoparticles, respectively (Figures S14 and S15 and Tables S3 and S4). At a low pH, ascorbic acid is only capable of reducing Au^{3+} to Au^+ (which form $Au(III)Cl_4^-$ and $Au(I)Cl_2^-$ in solution, respectively). The final reduction to Au^0 and the formation of nanoparticles may thus occur either by spontaneous disproportionation of $Au(I)Cl_2^-$ into $Au(III)Cl_4^-$ and Au^0, or *via* a redox reaction with the gel.[75] When performing both single-step and preloaded *in situ* growth on unmodified gelatin substrates (chemical structure shown in Figure 3A), AuNSt coatings were also produced with no other changes to the synthetic procedure (Figures 3D,E and S16). This result is relevant because it indicates that these syntheses may be broadly translatable to other biocompatible materials containing peptide bond structures (*e.g.,* collagen), and peptide or

https://doi.org/10.1021/acs.chemmater.4c00564
Chem. Mater. 2024, 36, 5192−5203

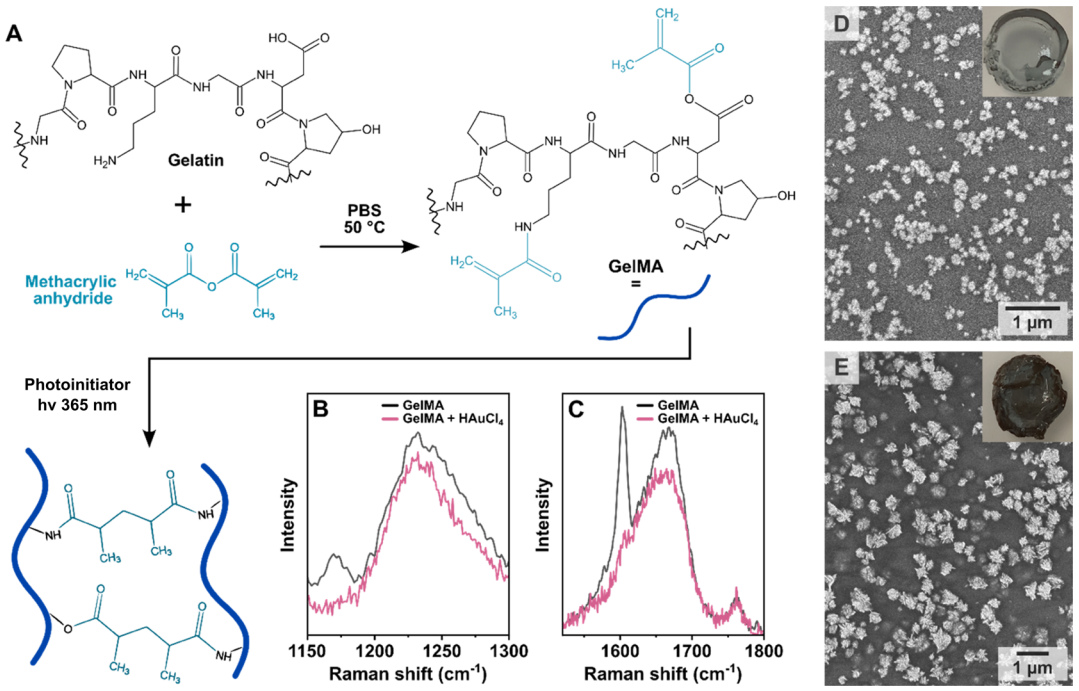

Figure 3. (A) Schematic representation of the reaction between gelatin and methacrylic anhydride to produce gelatin methacryloyl (GelMA) and subsequent GelMA cross-linking. (B, C) Raman scattering spectra showing changes in the characteristic GelMA peaks after incubation of the gel with $HAuCl_4$ for 24 h. SEM images of gold nanostars formed on 10% w/w gelatin (nonmethacrylated) by single-step (D) and preloaded (E) *in situ* growth (*insets:* digital photographs of gelatin substrates after AuNSt growth).

protein-based hydrogels), which would significantly expand the applicability of *in situ* growth.

We next evaluated whether *in situ* growth indeed leads to selective AuNSt formation on the gel surface. Nanocomposites containing colloidal AuNSt prelabeled with the Raman reporter 4-mercaptobenzoic acid (4-MBA) were prepared based on a previously reported method (Figures 4A and S17).[66] Nanocomposites with *in situ*-grown AuNSt were also prepared and incubated with 4-MBA. The spatial distributions of SERS signals at different depths for substrates containing labeled AuNSt were measured for the different preparations (Figure 4). Although high concentrations of AuNSt@4-MBA were used for the nanocomposites incorporating colloidal particles, SEM imaging showed few particles at the hydrogel surface (Figure 4B) and confocal SERS mapping yielded a uniform signal throughout the entire volume (Figure 4C, surface indicated with a white dashed line). On the other hand, confocal SERS confirmed that all the *in situ*-prepared samples exhibited the characteristic signal of 4-MBA at 1082 cm^{-1} primarily near the surface (Figure 4D–G). In some cases, extraneous SERS signals were present farther away from the surface, and SEM characterization of gel cross-sections did reveal the occasional presence of small groups of AuNSt at deeper locations (Figure S18), which would explain the SERS signal from those regions. However, SEM images of the cross-sections for all samples confirmed that the vast majority of AuNSt were present within the topmost few μm of the hydrogel, in agreement with SERS maps (Figures 4H–K and S19).

Plasmonic substrates functionalized with Raman reporters, *e.g.*, 4-MBA, are useful for bioimaging[35] and biosensing (pH, reactive oxygen species, *etc.*).[66,76,77] In this context, we next investigated whether surface localization of AuNSt would lead to an improvement of the SERS signal for substrate-bound Raman reporters due to a lower background scattering from the bulk of the gel and increased presence of plasmonic nanoparticles at the gel–solution interface. Our results indeed revealed that the SERS signal for 4-MBA was nearly 2 orders of magnitude higher for substrates prepared by the seed-mediated *in situ* growth methods (labeled LSB and TX) and ~1 order of magnitude higher for the single-step and preloaded *in situ* growth approaches (labeled single-step and preloaded, respectively), compared to a substrate prepared from presynthesized colloids (Figure 5A,B). Overall, the difference in SERS signals from seeded and seedless growth methods could be explained by a better match of their plasmonic response to the excitation laser line at 785 nm (Figure 5D). Previously reported simulations showed that an increased density of AuNSt does not afford significantly improved SERS enhancement factors (calculated as the intensity of the SERS signal divided by the Raman signal).[78] However, denser AuNSt coatings do increase the coverage of the Raman reporter, which would account for the difference in SERS signal between the nanocomposites prepared by single-step and preloaded seedless *in situ* growth.[62] In addition to the intensity, the SERS signals should also be as uniform as possible across the substrate, so we show that the spot-to-spot percent error is comparable between the colloidally prepared and *in situ* prepared nanocomposites (Figure 5C).

For completeness of the characterization of the various AuNSt-loaded hydrogels, we explored whether the incorporation of nanoparticles would disrupt the hydrogel network and its properties.[49,53,54] Rheological characterization was thus applied to the samples prepared by *in situ* growth (Figure S20 and Table S5). It was found that the values of the elastic storage modulus (G') for AuNSt composites prepared by *in situ* growth were more similar to those for native GelMA than for nanocomposites prepared by addition of colloidal particles.

https://doi.org/10.1021/acs.chemmater.4c00564
Chem. Mater. 2024, 36, 5192–5203

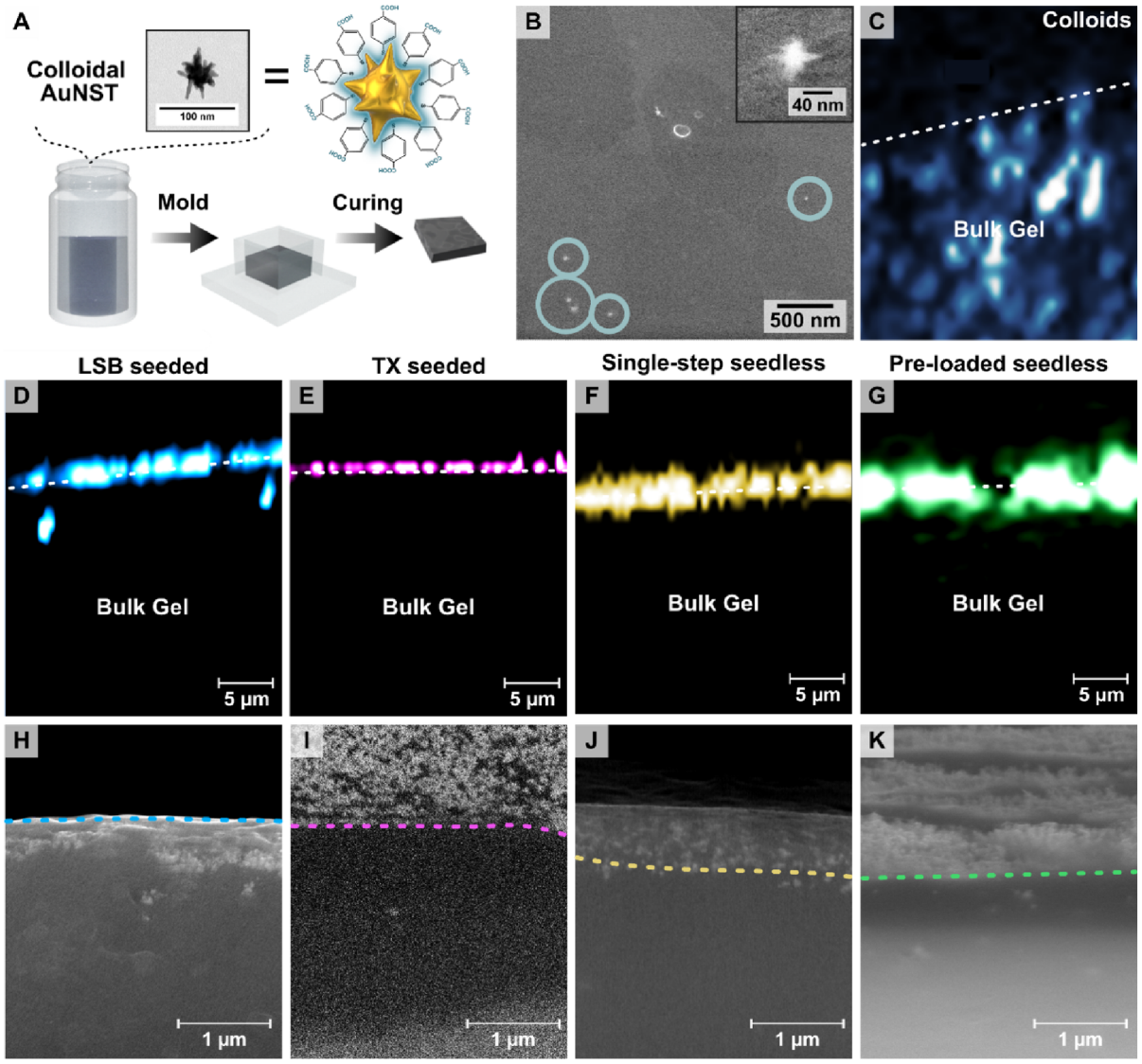

Figure 4. (A) Schematic showing the procedure for preparing hydrogels with 4-mercaptobenzoic acid labeled gold nanostars prepared in colloidal suspension. (B) SEM image showing the surface of a hydrogel mixed with a AuNSt colloid (=0.5 mM; Abs_{400} = 1.2). Few nanostars can be observed in the SEM images, indicated by blue circles. Surface-enhanced Raman scattering (SERS) depth slice maps (1−10 mW, 0.01−0.05 s integration; full details provided in the Supporting Information) showing the localization of the SERS signal corresponding to the characteristic peak of 4-mercaptobenzoic acid (4-MBA) at 1082 cm^{-1}, for substrates prepared using the different approaches: with colloidal nanostars (C), or seeded *in situ* growth using laruylsulfobetaine (LSB) (D) and Triton X-100 (TX) (E) as surfactants, single-step *in situ* growth (F), and preloaded *in situ* growth (G). SEM images showing the substrates in a cross-section profile for seeded *in situ* growth with LSB (H) and TX (I) as capping ligands, single-step *in situ* growth (J), and preloaded *in situ* growth (K) substrates. The visibility of the sample surface differs from sample to sample depending on the angle of the surface relative to the detector upon drying. Dashed lines were added as a guide to the eye, indicating the division between the internal part of the gel and the surface coated with nanostars. Low-magnification SEM images of the dried cross sections are shown in Figure S19.

This result indicates that the ability of the hydrogel to elastically store energy remains relatively unaffected when *in situ* growth is used, minimally affecting the gel's native physical properties.[79,80]

GelMA has also been applied as a substrate to support growth/differentiation and to study proliferation/invasion of stem and cancer cells, and is a usual component in 3D-printed cell culture scaffolds.[43,44,81,82] Prior works showed that incorporation of plasmonic nanoparticles in such schemes enable multimodal-bioimaging and SERS sensing.[35,49] Thus, we interrogated the possibility of using nanocomposites made by *in situ* growth for these applications, first demonstrating that AuNSt coatings could be prepared on 3D-printed GelMA scaffolds and subsequently seeding breast cancer cells (MDA-MB-231) on top of the scaffold for SERS studies. Whereas the high-density deposition of surfactant-free AuNSt specifically on the surface of 3D architectures is extremely challenging when starting from colloidal samples, it was found that *in situ* growth makes it possible to fabricate such coatings within less than 1 h. We 3D-printed GelMA scaffolds and subsequently incubated them in a growth solution, following the preloaded *in situ* growth procedure schematically described in Figure 2C. The successful coating of AuNSt on the scaffold's irregular features could be observed both by brightfield microscopy and SEM (Figure 6A−D). When the nanoparticles on the scaffold were functionalized with 4-MBA, SERS maps following the structure

https://doi.org/10.1021/acs.chemmater.4c00564
Chem. Mater. 2024, 36, 5192−5203

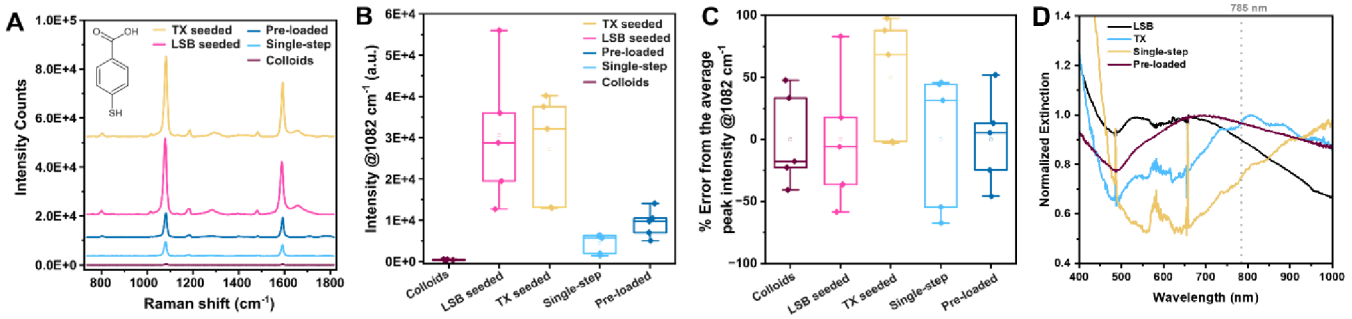

Figure 5. (A) Representative surface-enhanced Raman scattering (SERS) spectra for substrates prepared with colloidal nanostars ("colloids"), the seed-mediated *in situ* growth approaches with laurylsulfobetaine and Triton X-100 ("LSB" and "TX," respectively), single-step *in situ* growth, and preloaded *in situ* growth. (B) Comparison of the uniformity of the intensity of the peak corresponding to Raman reporter molecule 4-mercaptobenzoic acid (4-MBA) for the substrates made by each method (n = 5 for each). (C) Comparison of the percent error in the 4-MBA SERS signal (spectra taken at 7.1 mW (power at surface), 3 s accumulation, 50× long working distance objective, NA = 0.5). (D) Normalized UV−visible extinction spectra of the nanocomposites.

of the scaffold could be retrieved using 43.6 mW (power at surface measured after passing a 10× objective, NA = 0.25) and a short 0.01 s accumulation time. These parameters enabled faster large-area image acquisition, compared to recent studies on similar scaffolds,[49] again highlighting the utility of *in situ* growth substrates for SERS imaging.

Next, as a proof-of-concept biological application, GelMA scaffolds were 3D-printed and coated with AuNSt, following the preloaded synthesis procedure, and MDA-MB-231 cells were attached to the scaffolds. Instead of adding a Raman tag, a collagen/fibronectin layer was added to the scaffolds after AuNSt growth to promote cell seeding on the substrate (Figure 6E). We found that label-free sensing and 2D mapping of cells could be successfully performed without the addition of any Raman reporters. A quantifiable difference was identified in the density and morphology of cells on the scaffold, compared to the 2D cell culture. The cells adsorbed on the scaffold appeared to have a lower surface coverage and more rounded morphologies (average single cell area ≈300 μm^2 and 130 μm^2, in 2D and on the scaffold, respectively, both with and without AuNSt, Figure S20). However, viability evaluation 24 h postseeding *via* calcein-AM/propidium iodide staining for MDA-MB-231 cells showed similar results in the nanocomposite scaffolds, 2D culture and GelMA scaffolds without AuNSt (Figure S21). The 3D distribution of cells in the holes of the scaffold could also be clearly imaged by fluorescence confocal microscopy (Figure S22). Additionally, SERS spectra recorded from cell-containing regions showed distinct peaks, characteristic of unsaturated fatty acids found in the cell membrane, as well as amino acids (tyrosine or tryptophan/valine) at ∼1450 and 950 cm^{-1}, respectively. Other peaks at 520 and 450 cm^{-1} appeared more prominent at cell-containing regions, which may correspond to disulfide links present in proteins and wagging modes of carbonyl functional groups, possibly associated with the cell membrane, respectively.[83−85] However, there is also some evidence of these peaks in the spectra from off-cell regions (Figures 6G,S23 and S24). It should be stressed that, although different peaks were observed, the SERS map with the highest fidelity to the corresponding bright field image was built from the peak at ∼950 cm^{-1} (Figures 6H andS24). Ultimately, although the scaffold resolution, substrate material, and cell-adhesive coating require further optimization, our results show that *in situ* growth offers a pathway to the fabrication of complex plasmonic nanoparticle-hydrogel materials with tunable properties with potential for various applications, especially labeled and label-free chemical and biological sensing and bioimaging.

4. CONCLUSIONS

We demonstrated the possibility to translate *in situ* synthesis of AuNSt onto hydrogel substrates (GelMA), applying both seed-mediated *in situ* overgrowth and direct *in situ* growth, without any colloidal presynthesis steps. The unconventional synthetic methods developed here produce dense AuNSt coatings selectively near the surface of the polymer material. Furthermore, the developed nanocomposites are characterized by up to ∼100× higher SERS signals than similar materials prepared from colloids. The versatility of the *in situ* growth method for targeting substrates with different geometries was demonstrated, and dense layers of AuNSt were created on complex substrates with 3D features within minutes, which is difficult to achieve using colloid-based approaches. The high SERS signals from AuNSt labeled with a Raman reporter molecule enabled rapid image acquisition of 3D scaffolds and proof-of-concept tests applying these substrates for label-free biological sensing and imaging were also realized. The results of this work highlight the ease and tunability of *in situ* wet-chemical fabrication for creating nanoparticle coatings on soft polymers, which can be useful for a wide range of applications, including chemical and biological sensing, and SERS imaging.

Looking ahead, although surfactant-free syntheses are attractive for biological applications, the highest SERS signals were observed when using seeded growth. Thus, to further improve the yield and uniformity of the surfactant-free growth, and consequently the SERS performance, we envisage a two-step method where the spatiotemporal separation of nucleation and growth is replicated. Moreover, unlike with hard substrates, the ability to widely tune the chemical and physical properties/compositions of the gels allows us to explore synthetic routes that might be helpful toward the growth of particles with different shapes. Future studies will also pursue the translation of *in situ* AuNSt growth on different peptide-containing polymers. Overall, the fabrication method presented herein will be useful in instances where the plasmonic nanoparticles must be readily accessible at interfaces, such as for studying analytes that cannot penetrate gel structures (e.g., macromolecules and/or hydrophobic species), grafted 2D cell cultures (either with label or label-free), or tissues.

https://doi.org/10.1021/acs.chemmater.4c00564
Chem. Mater. 2024, 36, 5192−5203

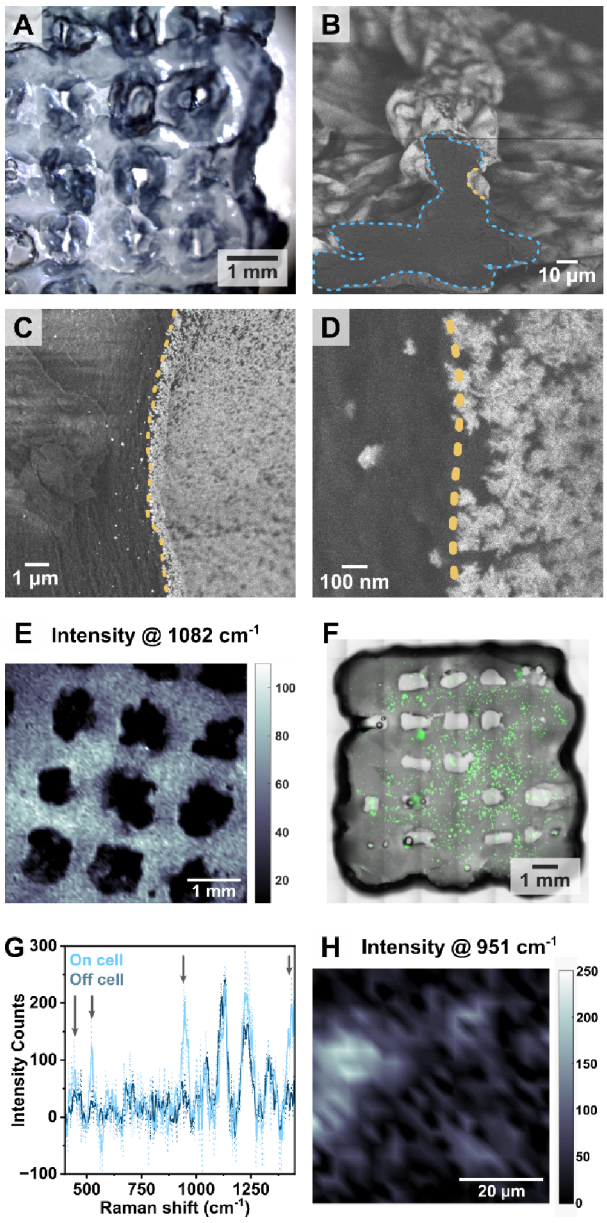

Figure 6. (A) Digital photograph showing an entire 3D scaffold with irregular surface features coated with gold nanostars (AuNSt), which provide a dark blue color. (B−D) SEM images of a cross-section of the scaffold. Cross-section areas are indicated by dashed lines. A specific region of interest at the cross-section edge common to all images is indicated by yellow dashed lines. (E) SERS *x*,*y*-map of a scaffold functionalized with 4-mercaptobenzoic acid (10× objective, NA = 0.25, 43.6 mW, 0.01 s accumulation). (F) Fluorescence confocal microscopy images of green fluorescence protein (GFP)-expressing MDA-MB-231 breast cancer cells seeded on a AuNSt scaffold functionalized with collagen/fibronectin. (G) Representative SERS spectra off and on the cells (differences indicated by arrows). (H) SERS map of seeded cells, based on the intensity at 951 cm^{-1}. Additional fluorescence microscopy images and cell viability evaluation in 2D and 3D are shown in Figures S21 and S22, and additional SERS characterization is provided in Figures S23 and S24.

■ ASSOCIATED CONTENT

Supporting Information

The Supporting Information is available free of charge at https://pubs.acs.org/doi/10.1021/acs.chemmater.4c00564.

Additional details on nanoparticle fabrication and complementary characterization of the nanocomposites; Figure S1−S24: characterization for seed-mediated *in situ* growth with TX and LSB; characterization for single-step *in situ* growth; characterization for pre-loaded *in situ* growth; characterization of GelMA interaction with gold; characterization for the SERS measurements; rheological characterization; characterization from cell viability tests (PDF)

■ AUTHOR INFORMATION

Corresponding Authors

Gail A. Vinnacombe-Willson − *CIC biomaGUNE, Basque Research and Technology Alliance (BRTA), Donostia-San Sebastián 20014, Spain*; Email: gvinnacombe@cicbiomagune.es

Luis M. Liz-Marzán − *CIC biomaGUNE, Basque Research and Technology Alliance (BRTA), Donostia-San Sebastián 20014, Spain; Centro de Investigación Biomédica en Red de Bioingeniería Biomateriales, y Nanomedicina (CIBER-BBN), Donostia-San Sebastián 20014, Spain; Ikerbasque Basque Foundation for Science, Bilbao 48009, Spain; Cinbio, Universidade de Vigo, Vigo 36310, Spain*; orcid.org/0000-0002-6647-1353; Email: llizmarzan@cicbiomagune.es

Authors

Clara García-Astrain − *CIC biomaGUNE, Basque Research and Technology Alliance (BRTA), Donostia-San Sebastián 20014, Spain; Centro de Investigación Biomédica en Red de Bioingeniería Biomateriales, y Nanomedicina (CIBER-BBN), Donostia-San Sebastián 20014, Spain*; orcid.org/0000-0002-4231-7335

Lara Troncoso-Afonso − *CIC biomaGUNE, Basque Research and Technology Alliance (BRTA), Donostia-San Sebastián 20014, Spain; Department of Applied Chemistry, University of the Basque Country (UPV-EHU), Donostia-San Sebastián 20018, Spain*; orcid.org/0009-0004-0695-3248

Marita Wagner − *CIC biomaGUNE, Basque Research and Technology Alliance (BRTA), Donostia-San Sebastián 20014, Spain; Department of Applied Chemistry, University of the Basque Country (UPV-EHU), Donostia-San Sebastián 20018, Spain; CIC nanoGUNE, Basque Research and Technology Alliance (BRTA), Donostia-San Sebastián 20018, Spain*

Judith Langer − *CIC biomaGUNE, Basque Research and Technology Alliance (BRTA), Donostia-San Sebastián 20014, Spain*; orcid.org/0000-0003-3527-5728

Patricia González-Callejo − *CIC biomaGUNE, Basque Research and Technology Alliance (BRTA), Donostia-San Sebastián 20014, Spain*

Desirè Di Silvio − *CIC biomaGUNE, Basque Research and Technology Alliance (BRTA), Donostia-San Sebastián 20014, Spain*

Complete contact information is available at: https://pubs.acs.org/10.1021/acs.chemmater.4c00564

Author Contributions

The experiments were designed by G.A.V.-W., L.M., L.-M. and G.A.V.-W., with assistance from M.W.; performed and developed the synthetic approaches; and carried out optical and electron microscopy characterization. Rheological charac-

https://doi.org/10.1021/acs.chemmater.4c00564
Chem. Mater. 2024, 36, 5192−5203

terization and NMR were performed by C.G.A., and L.T-.A., G.A.V.-W., and J.L. performed the SERS characterization. G.A.V.-W. and P.G.C. led the cell experiments and fluorescence microscopy measurements. D.D.S. performed the XPS experiments. The manuscript was written by G.A.V.-W. with contributions from all authors. All authors have given approval to the final version of the manuscript.

Notes

The authors declare no competing financial interest.

■ ACKNOWLEDGMENTS

This work was funded by the European Research Council (ERC Advanced Grant 787510, 4DbioSERS). C.G.A. thanks the Spanish State Research Agency for a Juan de la Cierva Incorporación Fellowship (IJC2019-040827-I). L.T.A. thanks the Spanish Ministry of Universities for a Formación de Profesorado Universitario Fellowship (FPU-05867). The authors thank Dr. Marco Möller and the CIC biomaGUNE technological platform, as well as Dr. Christopher Tollan and the CIC nanoGUNE technological platform for assistance with scanning electron microscopy characterization. We also thank Dr. Carlos Renero-Lecuna and Dr. Leonardo Scarabelli for their helpful advice on optical characterization and synthesis, respectively.

■ REFERENCES

(1) Pallares, R. M.; Stilson, T.; Choo, P.; Hu, J.; Odom, T. W. Using Good's Buffers To Control the Anisotropic Structure and Optical Properties of Spiky Gold Nanoparticles for Refractive Index Sensing. *ACS Appl. Nano Mater.* **2019**, *2* (8), 5266−5271.

(2) Langer, J.; Jimenez de Aberasturi, D.; Aizpurua, J.; Alvarez-Puebla, R. A.; Auguié, B.; Baumberg, J. J.; Bazan, G. C.; Bell, S. E. J.; Boisen, A.; Brolo, A. G.; et al.et al. Present and Future of Surface-Enhanced Raman Scattering. *ACS Nano* **2020**, *14*, 28−117.

(3) Plou, J.; Valera, P. S.; García, I.; de Albuquerque, C. D. L.; Carracedo, A.; Liz-Marzán, L. M. Prospects of Surface-Enhanced Raman Spectroscopy for Biomarker Monitoring toward Precision Medicine. *ACS Photonics.* **2022**, *9*, 333−350.

(4) Liu, Y.; Chorniak, E.; Odion, R.; Etienne, W.; Nair, S. K.; Maccarini, P.; Palmer, G. M.; Inman, B. A.; Vo-Dinh, T. Plasmonic Gold Nanostars for Synergistic Photoimmunotherapy to Treat Cancer. *Nanophotonics* **2021**, *10*, 3295−3302.

(5) de la Encarnación, C.; Jimenez de Aberasturi, D.; Liz-Marzán, L. M. Multifunctional Plasmonic-Magnetic Nanoparticles for Bioimaging and Hyperthermia. *Adv. Drug Delivery Rev.* **2022**, *189*, 114484−114502.

(6) de la Encarnación, C.; Lenzi, E.; Henriksen-Lacey, M.; Molina, B.; Jenkinson, K.; Herrero, A.; Colás, L.; Ramos-Cabrer, P.; Toro-Mendoza, J.; Orue, I.; et al.et al. Hybrid Magnetic−Plasmonic Nanoparticle Probes for Multimodal Bioimaging. *J. Phys. Chem. C* **2022**, *126*, 19519−19531.

(7) Andreiuk, B.; Nicolson, F.; Clark, L. M.; Panikkanvalappil, S. R.; Kenry; Rashidian, M.; Harmsen, S.; Kircher, M. F. Design and Synthesis of Gold Nanostars-Based SERS Nanotags for Bioimaging Applications. *Nanotheranostics* **2022**, *6* (1), 10−30.

(8) Zhu, S.; Deng, B.; Liu, F.; Li, J.; Lin, L.; Ye, J. Surface-Enhanced Raman Scattering Bioimaging with an Ultrahigh Signal-to-Background Ratio under Ambient Light. *ACS Appl. Mater. Interfaces* **2022**, *14*, 8876−8887.

(9) Peng, C.; Xu, J.; Yu, M.; Ning, X.; Huang, Y.; Du, B.; Hernandez, E.; Kapur, P.; Hsieh, J.-T.; Zheng, J. Tuning the In Vivo Transport of Anticancer Drugs Using Renal-Clearable Gold Nanoparticles. *Angew. Chem., Int. Ed.* **2019**, *58*, 8479−8483.

(10) Luther, D. C.; Huang, R.; Jeon, T.; Zhang, X.; Lee, Y.-W.; Nagaraj, H.; Rotello, V. M. Delivery of Drugs, Proteins, and Nucleic Acids Using Inorganic Nanoparticles. *Adv. Drug Delivery Rev.* **2020**, *156*, 188−213.

(11) Zhang, S.; Chen, C.; Xue, C.; Chang, D.; Xu, H.; Salena, B. J.; Li, Y.; Wu, Z.-S. Ribbon of DNA Lattice on Gold Nanoparticles for Selective Drug Delivery to Cancer Cells. *Angew. Chem., Int. Ed.* **2020**, *59*, 14584−14592.

(12) Lv, S.-W.; Liu, Y.; Xie, M.; Wang, J.; Yan, X.-W.; Li, Z.; Dong, W.-G.; Huang, W.-H. Near-Infrared Light-Responsive Hydrogel for Specific Recognition and Photothermal Site-Release of Circulating Tumor Cells. *ACS Nano* **2016**, *10*, 6201−6210.

(13) Dong, J.; Chen, J.-F.; Smalley, M.; Zhao, M.; Ke, Z.; Zhu, Y.; Tseng, H.-R. Nanostructured Substrates for Detection and Characterization of Circulating Rare Cells: From Materials Research to Clinical Applications. *Adv. Mater.* **2020**, *32*, 1903663−1903701.

(14) Merkel, T. J.; Herlihy, K. P.; Nunes, J.; Orgel, R. M.; Rolland, J. P.; DeSimone, J. Shape-Specific Top-Down Fabrication Methods for the Synthesis of Engineered Colloidal Particles. *Langmuir* **2010**, *26* (16), 13086−13096.

(15) Kasani, S.; Curtin, K.; Wu, N. A Review of 2D and 3D Plasmonic Nanostructure Array Patterns: Fabrication, Light Management and Sensing Applications. *Nanophotonics* **2019**, *8*, 2065−2089.

(16) Scarabelli, L.; Vila-Liarte, D.; Mihi, A.; Liz-Marzán, L. M. Templated Colloidal Self-Assembly for Lattice Plasmon Engineering. *Acc. Mater. Res.* **2021**, *2*, 816−827.

(17) Brasse, Y.; Gupta, V.; Schollbach, H. C. T.; Karg, M.; König, T. A. F.; Fery, A. Mechanotunable Plasmonic Properties of Colloidal Assemblies. *Adv. Mater. Interfaces* **2020**, *7*, 1901678−1901693.

(18) Tagliabue, G.; Jermyn, A. S.; Sundararaman, R.; Welch, A. J.; DuChene, J. S.; Pala, R.; Davoyan, A. R.; Narang, P.; Atwater, H. A. Quantifying the Role of Surface Plasmon Excitation and Hot Carrier Transport in Plasmonic Devices. *Nat. Commun.* **2018**, *9*, 3394.

(19) Liz-Marzán, L. M. *Colloidal Synthesis of Plasmonic Nanometals*; CRC Press, 2020.

(20) Scarabelli, L.; Sánchez-Iglesias, A.; Pérez-Juste, J.; Liz-Marzán, L. M. A "Tips and Tricks" Practical Guide to the Synthesis of Gold Nanorods. *J. Phys. Chem. Lett.* **2015**, *6*, 4270−4279.

(21) Yuan, H.; Khoury, C. G.; Hwang, H.; Wilson, C. M.; Grant, G. A.; Vo-Dinh, T. Gold Nanostars: Surfactant-Free Synthesis, 3D Modelling, and Two-Photon Photoluminescence Imaging. *Nanotechnology* **2012**, *23*, 075102.

(22) Boles, M. A.; Engel, M.; Talapin, D. V. Self-Assembly of Colloidal Nanocrystals: From Intricate Structures to Functional Materials. *Chem. Rev.* **2016**, *116*, 11220−11289.

(23) Deng, K.; Luo, Z.; Tan, L.; Quan, Z. Self-Assembly of Anisotropic Nanoparticles into Functional Superstructures. *Chem. Soc. Rev.* **2020**, *49*, 6002−6038.

(24) Vinnacombe-Willson, G. A.; Conti, Y.; Stefancu, A.; Weiss, P. S.; Cortés, E.; Scarabelli, L. Direct Bottom-Up *In Situ* Growth: A Paradigm Shift for Studies in Wet-Chemical Synthesis of Gold Nanoparticles. *Chem. Rev.* **2023**, *123*, 8488−8529.

(25) Liu, G.; Zhang, C.; Wu, J.; Mirkin, C. A. Using Scanning-Probe Block Copolymer Lithography and Electron Microscopy To Track Shape Evolution in Multimetallic Nanoclusters. *ACS Nano* **2015**, *9*, 12137−12145.

(26) Demille, T. B.; Hughes, R. A.; Neretina, S. Periodic Arrays of Dewetted Silver Nanostructures on Sapphire and Quartz: Effect of Substrate Truncation on the Localized Surface Plasmon Resonance and Near-Field Enhancement. *J. Phys. Chem. C* **2019**, *123*, 19879−19886.

(27) Demille, T. B.; Hughes, R. A.; Dominique, N.; Olson, J. E.; Rouvimov, S.; Camden, J. P.; Neretina, S. Large-Area Periodic Arrays of Gold Nanostars Derived from HEPES-, DMF-, and Ascorbic-Acid-Driven Syntheses. *Nanoscale* **2020**, *12*, 16489−16500.

(28) Jia, J.; Metzkow, N.; Park, S.-M.; Wu, Y. L.; Sample, A. D.; Diloknawarit, B.; Jung, I.; Odom, T. W. Spike Growth on Patterned Gold Nanoparticle Scaffolds. *Nano Lett.* **2023**, *23*, 11260−11265.

(29) Vinnacombe-Willson, G. A.; Chiang, N.; Scarabelli, L.; Hu, Y.; Heidenreich, L. K.; Li, X.; Gong, Y.; Inouye, D. T.; Fisher, T. S.; Weiss, P. S.; et al.et al. *In Situ* Shape Control of Thermoplasmonic

https://doi.org/10.1021/acs.chemmater.4c00564
Chem. Mater. 2024, 36, 5192−5203

Gold Nanostars on Oxide Substrates for Hyperthermia-Mediated Cell Detachment. *ACS Cent. Sci.* **2020**, *6*, 2105−2116.
(30) Fortuni, B.; Inose, T.; Uezono, S.; Toyouchi, S.; Umemoto, K.; Sekine, S.; Fujita, Y.; Ricci, M.; Lu, G.; Masuhara, A.; et al.et al. *In Situ* Synthesis of Au-Shelled Ag Nanoparticles on PDMS for Flexible, Long-Life, and Broad Spectrum-Sensitive SERS Substrates. *Chem. Commun.* **2017**, *53*, 11298−11301.
(31) Fortuni, B.; Fujita, Y.; Ricci, M.; Inose, T.; Aubert, R.; Lu, G.; Hutchison, J. A.; Hofkens, J.; Latterini, L.; Uji-I, H. A Novel Method for *in Situ* Synthesis of SERS-Active Gold Nanostars on Polydimethylsiloxane Film. *Chem. Commun.* **2017**, *53*, 5121−5124.
(32) Vinnacombe-Willson, G. A.; Conti, Y.; Jonas, S. J.; Weiss, P. S.; Mihi, A.; Scarabelli, L. Surface Lattice Plasmon Resonances by Direct *in Situ* Substrate Growth of Gold Nanoparticles in Ordered Arrays. *Adv. Mater.* **2022**, *34*, 2205330−2205341.
(33) Vinnacombe-Willson, G. A.; Lee, J. K.; Chiang, N.; Scarabelli, L.; Yue, S.; Foley, R.; Frost, I.; Weiss, P. S.; Jonas, S. J. Exploring the Bottom-Up Growth of Anisotropic Gold Nanoparticles from Substrate-Bound Seeds in Microfluidic Reactors. *ACS Appl. Nano Mater.* **2023**, *6* (8), 6454−6460.
(34) Pastoriza-Santos, I.; Kinnear, C.; Pérez-Juste, J.; Mulvaney, P.; Liz-Marzán, L. M. Plasmonic Polymer Nanocomposites. *Nat. Rev. Mater.* **2018**, *3*, 375−391.
(35) Lenzi, E.; Jimenez de Aberasturi, D.; Henriksen-Lacey, M.; Piñeiro, P.; Muniz, A. J.; Lahann, J.; Liz-Marzán, L. M. SERS and Fluorescence-Active Multimodal Tessellated Scaffolds for Three-Dimensional Bioimaging. *ACS Appl. Mater. Interfaces* **2022**, *14*, 20708−20719.
(36) Plou, J.; Molina-Martínez, B.; García-Astrain, C.; Langer, J.; García, I.; Ercilla, A.; Perumal, G.; Carracedo, A.; Liz-Marzán, L. M. Nanocomposite Scaffolds for Monitoring of Drug Diffusion in Three-Dimensional Cell Environments by Surface-Enhanced Raman Spectroscopy. *Nano Lett.* **2021**, *21*, 8785−8793.
(37) Yue, K.; Trujillo-de Santiago, G.; Alvarez, M. M.; Tamayol, A.; Annabi, N.; Khademhosseini, A. Synthesis, properties, and biomedical applications of gelatin methacryloyl (GelMA) hydrogels. *Biomaterials* **2015**, *73*, 254−271.
(38) Piao, Y.; You, H.; Xu, T.; Bei, H.-P.; Piwko, I. Z.; Kwan, Y. Y.; Zhao, X. Biomedical Applications of Gelatin Methacryloyl Hydrogels. *Engin. Regen.* **2021**, *2*, 47−56.
(39) Neves, M. I.; Moroni, L.; Barrias, C. C. Modulating Alginate Hydrogels for Improved Biological Performance as Cellular 3D Microenvironments. *Front. Bioeng. Biotechnol.* **2020**, *8*, 665.
(40) Lin, K.; Zhang, D.; Macedo, M. H.; Cui, W.; Sarmento, B.; Shen, G. Advanced Collagen-based Biomaterials for Regenerative Biomedicine. *Adv. Funct. Mater.* **2019**, *29*, 1804943−1804949.
(41) Seidlits, S. K.; Khaing, Z. Z.; Petersen, R. R.; Nickels, J. D.; Vanscoy, J. E.; Shear, J. B.; Schmidt, C. E. The Effects of Hyaluronic Acid Hydrogels with Tunable Mechanical Properties on Neural Progenitor Cell Differentiation. *Biomaterials* **2010**, *31*, 3930−3940.
(42) Kurian, A. G.; Singh, R. K.; Patel, K. D.; Lee, J.-H.; Kim, H.-W. Multifunctional GelMA Platforms with Nanomaterials for Advanced Tissue Therapeutics. *Bioactive Mater.* **2022**, *8*, 267−295.
(43) Duan, J.; Cao, Y.; Shen, Z.; Cheng, Y.; Ma, Z.; Wang, L.; Zhang, Y.; An, Y.; Sang, S. 3D Bioprinted GelMA/PEGDA Hybrid Scaffold for Establishing an in Vitro Model of Melanoma. *J. Microbiol. Biotechnol.* **2022**, *32*, 531−540.
(44) Blanco-Fernandez, B.; Rey-Vinolas, S.; Bağcı, G.; Rubi-Sans, G.; Otero, J.; Navajas, D.; Perez-Amodio, S.; Engel, E. Bioprinting Decellularized Breast Tissue for the Development of Three-Dimensional Breast Cancer Models. *ACS Appl. Mater. Interfaces* **2022**, *14*, 29467−29482.
(45) Erdem, A.; Darabi, M. A.; Nasiri, R.; Sangabathuni, S.; Ertas, Y. N.; Alem, H.; Hosseini, V.; Shamloo, A.; Nasr, A. S.; Ahadian, S.; et al.et al. 3D Bioprinting of Oxygenated Cell-Laden Gelatin Methacryloyl Constructs. *Adv. Healthcare Mater.* **2020**, *9*, 1901794−1901806.
(46) Zhu, J.; Zhou, X.; Kim, H.-J.; Qu, M.; Jiang, X.; Lee, K.; Ren, L.; Wu, Q.; Wang, C.; Zhu, X.; et al.et al. Gelatin Methacryloyl Microneedle Patches for Minimally Invasive Extraction of Skin Interstitial Fluid. *Small* **2020**, *16*, 1905910−1905919.
(47) Carvalho, B. G.; Nakayama, A.; Miwa, H.; Han, S. W.; de la Torre, L. G.; Di Carlo, D.; Lee, J.; Kim, H.-J.; Khademhosseini, A.; de Barros, N. R. Gelatin Methacryloyl Granular Scaffolds for Localized mRNA Delivery. *Aggregate* **2024**, *5*, No. e464.
(48) Vázquez-Aristizabal, P.; Perumal, G.; García-Astrain, C.; Liz-Marzán, L. M.; Izeta, A. Trends in Tissue Bioprinting, Cell-Laden Bioink Formulation, and Cell Tracking. *ACS Omega* **2022**, *7*, 16236−16243.
(49) García-Astrain, C.; Lenzi, E.; Jimenez de Aberasturi, D.; Henriksen-Lacey, M.; Binelli, M. R.; Liz-Marzán, L. M. 3D-Printed Biocompatible Scaffolds with Built-In Nanoplasmonic Sensors. *Adv. Funct. Mater.* **2020**, *30*, 2005407−2005418.
(50) Eyimegwu, P. N.; Lartey, J. A.; Kim, J.-H. Gold-Nanoparticle-Embedded Poly(N-Isopropylacrylamide) Microparticles for Selective Quasi-Homogeneous Catalytic Homocoupling Reactions. *ACS Appl. Nano Mater.* **2019**, *2*, 6057−6066.
(51) Jang, W.; Taylor IV, R.; Eyimegwu, P. N.; Byun, H.; Kim, J. In Situ Formation of Gold Nanoparticles within a Polymer Particle and Their Catalytic Activities in Various Chemical Reactions. *ChemPhyschem* **2019**, *20*, 70−77.
(52) Egemole, F. O.; Eyimegwu, F. M.; Yun, J.; Jang, W.; Byun, H.; Hou, J.; Kim, J.-H. Effects of Crosslinking Density on the *In Situ* Formation of Gold-Polymer Composite Particles and Their Catalytic Properties. *Coll. Surf. A* **2022**, *640*, 128409−128418.
(53) Wang, C.; Flynn, N. T.; Langer, R. Controlled Structure and Properties of Thermoresponsive Nanoparticle−Hydrogel Composites. *Adv. Mater.* **2004**, *16*, 1074−1079.
(54) Tsuge, Y.; Moriya, T.; Moriyama, Y.; Tokura, Y.; Shiratori, S. Slippery Liquid-Immobilized Coating Films Using *in Situ* Oxidation−Reduction Reactions of Metal Ions in Polyelectrolyte Films. *ACS Appl. Mater. Interfaces* **2017**, *9*, 15122−15129.
(55) Chung, M.; Skinner, W. H.; Robert, C.; Campbell, C. J.; Rossi, R. M.; Koutsos, V.; Radacsi, N. Fabrication of a Wearable Flexible Sweat pH Sensor Based on SERS-Active Au/TPU Electrospun Nanofibers. *ACS Appl. Mater. Interfaces* **2021**, *13*, 51504−51518.
(56) Abdelmoti, L. G.; Zamborini, F. P. Potential-Controlled Electrochemical Seed-Mediated Growth of Gold Nanorods Directly on Electrode Surfaces. *Langmuir* **2010**, *26*, 13511−13521.
(57) Kukhta, A.; Pochtenny, A.; Misevich, A.; Kukhta, I.; Semenova, E.; Vorobyova, S.; Sarantopoulou, E. Optical and Electrophysical Properties of Nanocomposites Based on PEDOT: PSS and Gold/Silver Nanoparticles. *Phys. Solid State.* **2014**, *56*, 827−834.
(58) Soares, A. L.; Hryniewicz, B. M.; Deller, A. E.; Volpe, J.; Marchesi, L. F.; Souto, D. E.; Vidotti, M. Electrodes Based on PEDOT Nanotubes Decorated with Gold Nanoparticles for Biosensing and Energy Storage. *ACS Appl. Nano Mater.* **2021**, *4*, 9945−9956.
(59) Nambiar, H. N.; Zamborini, F. P. Size-Dependent Electrochemical Metal Growth Kinetics. *J. Phys. Chem. C* **2023**, *127*, 4087−4095.
(60) Hao, F.; Nehl, C. L.; Hafner, J. H.; Nordlander, P. Plasmon Resonances of a Gold Nanostar. *Nano Lett.* **2007**, *7*, 729−732.
(61) Baffou, G.; Cichos, F.; Quidant, R. Applications and Challenges of Thermoplasmonics. *Nat. Mater.* **2020**, *19*, 946−958.
(62) Khoury, C. G.; Vo-Dinh, T. Gold Nanostars for Surface-Enhanced Raman Scattering: Synthesis, Characterization and Optimization. *J. Phys. Chem. C* **2008**, *112*, 18849−18859.
(63) Van Den Bulcke, A. I.; Bogdanov, B.; De Rooze, N.; Schacht, E. H.; Cornelissen, M.; Berghmans, H. Structural and Rheological Properties of Methacrylamide Modified Gelatin Hydrogels. *Biomacromolecules* **2000**, *1*, 31−38.
(64) Arya, A. D.; Hallur, P. M.; Karkisaval, A. G.; Gudipati, A.; Rajendiran, S.; Dhavale, V.; Ramachandran, B.; Jayaprakash, A.; Gundiah, N.; Chaubey, A. Gelatin Methacrylate Hydrogels as Biomimetic Three-Dimensional Matrixes for Modeling Breast Cancer Invasion and Chemoresponse in Vitro. *ACS Appl. Mater. Interfaces* **2016**, *8*, 22005−22017.

(65) Celikkin, N.; Mastrogiacomo, S.; Jaroszewicz, J.; Walboomers, X. F.; Swieszkowski, W. Gelatin Methacrylate Scaffold for Bone Tissue Engineering: The Influence of Polymer Concentration. *J. Biomed. Mater. Res., Part A* **2018**, *106*, 201−209.
(66) Zhang, Y.; Jimenez de Aberasturi, D.; Henriksen-Lacey, M.; Langer, J.; Liz-Marzán, L. M. Live-Cell Surface-Enhanced Raman Spectroscopy Imaging of Intracellular pH: From Two Dimensions to Three Dimensions. *ACS Sens.* **2020**, *5*, 3194−3206.
(67) Casu, A.; Cabrini, E.; Donà, A.; Falqui, A.; Diaz-Fernandez, Y.; Milanese, C.; Taglietti, A.; Pallavicini, P. Controlled Synthesis of Gold Nanostars by Using a Zwitterionic Surfactant. *Chem. - Eur. J.* **2012**, *18*, 9381−9390.
(68) Pallavicini, P.; Donà, A.; Casu, A.; Chirico, G.; Collini, M.; Dacarro, G.; Falqui, A.; Milanese, C.; Sironi, L.; Taglietti, A. Triton X-100 for Three-Plasmon Gold Nanostars with Two Photothermally Active NIR (near IR) and SWIR (Short-Wavelength IR) Channels. *Chem. Commun.* **2013**, *49*, 6265−6267.
(69) Pastoriza-Santos, I.; Liz-Marzán, L. M. Formation of PVP-Protected Metal Nanoparticles in DMF. *Langmuir* **2002**, *18*, 2888−2894.
(70) Atta, S.; Beetz, M.; Fabris, L. Understanding the Role of $AgNO_3$ Concentration and Seed Morphology in the Achievement of Tunable Shape Control in Gold Nanostars. *Nanoscale* **2019**, *11*, 2946−2958.
(71) Turkevich, J.; Stevenson, P. C.; Hillier, J. A Study of the Nucleation and Growth Processes in the Synthesis of Colloidal Gold. *Discuss. Faraday Soc.* **1951**, *11*, 55−75.
(72) Frens, G. Controlled Nucleation for the Regulation of the Particle Size in Monodisperse Gold Suspensions. *Nat. Phys. Sci.* **1973**, *241*, 20−22.
(73) Odom, T. W.; Nehl, C. L. How Gold Nanoparticles Have Stayed in the Light: The 3M's Principle. *ACS Nano* **2008**, *2*, 612−616.
(74) Barbosa, S.; Agrawal, A.; Rodríguez-Lorenzo, L.; Pastoriza-Santos, I.; Alvarez-Puebla, R. A.; Kornowski, A.; Weller, H.; Liz-Marzán, L. M. Tuning Size and Sensing Properties in Colloidal Gold Nanostars. *Langmuir* **2010**, *26*, 14943−14950.
(75) Goerlitzer, E. S. A.; Kunz, U.; Vogel, N.; Engstler, J.; Andrieu-Brunsen, A. N-Methyl-2-Pyrrolidone as a Reaction Medium for Gold(III)-Ion Reduction and Star-like Gold Nanostructure Formation. *ACS Omega* **2022**, *7*, 9484−9495.
(76) Williams, A.; Flynn, K. J.; Xia, Z.; Dunstan, P. R. Multivariate Spectral Analysis of pH SERS Probes for Improved Sensing Capabilities. *J. Raman Spectrosc.* **2016**, *47*, 819−827.
(77) Kumar, S.; Kumar, A.; Kim, G.; Rhim, W.; Hartman, K. L.; Nam, J. Myoglobin and Polydopamine-engineered Raman Nanoprobes for Detecting, Imaging, and Monitoring Reactive Oxygen Species in Biological Samples and Living Cells. *Small* **2017**, *13*, 1701584−1701594.
(78) Solís, D. M.; Taboada, J. M.; Obelleiro, F.; Liz-Marzán, L. M.; García de Abajo, F. J. Optimization of Nanoparticle-Based SERS Substrates through Large-Scale Realistic Simulations. *ACS Photonics.* **2017**, *4*, 329−337.
(79) Li, L.; Gil, C. J.; Finamore, T. A.; Evans, C. J.; Tomov, M. L.; Ning, L.; Theus, A.; Kabboul, G.; Serpooshan, V.; Roeder, R. K. Methacrylate-Modified Gold Nanoparticles Enable Noninvasive Monitoring of Photocrosslinked Hydrogel Scaffolds. *Adv. Nano-Biomed Res.* **2022**, *2*, 2200022−2200037.
(80) Heo, D. N.; Ko, W.-K.; Bae, M. S.; Lee, J. B.; Lee, D.-W.; Byun, W.; Lee, C. H.; Kim, E.-C.; Jung, B.-Y.; Kwon, I. K. Enhanced Bone Regeneration with a Gold Nanoparticle−Hydrogel Complex. *J. Mater. Chem. B* **2014**, *2*, 1584−1593.
(81) Fan, L.; Liu, C.; Chen, X.; Zou, Y.; Zhou, Z.; Lin, C.; Tan, G.; Zhou, L.; Ning, C.; Wang, Q. Directing Induced Pluripotent Stem Cell Derived Neural Stem Cell Fate with a Three-Dimensional Biomimetic Hydrogel for Spinal Cord Injury Repair. *ACS Appl. Mater. Interfaces* **2018**, *10*, 17742−17755.
(82) Cui, H.; Esworthy, T.; Zhou, X.; Hann, S. Y.; Glazer, R. I.; Li, R.; Zhang, L. G. Engineering a Novel 3D Printed Vascularized Tissue Model for Investigating Breast Cancer Metastasis to Bone. *Adv. Healthcare Mater.* **2020**, *9*, 1900924−1900935.
(83) Contorno, S.; Darienzo, R. E.; Tannenbaum, R. Evaluation of Aromatic Amino Acids as Potential Biomarkers in Breast Cancer by Raman Spectroscopy Analysis. *Sci. Rep.* **2021**, *11*, 1698.
(84) Hartsuiker, L.; Zeijen, N. J.; Terstappen, L. W.; Otto, C. A Comparison of Breast Cancer Tumor Cells with Varying Expression of the Her2/Neu Receptor by Raman Microspectroscopic Imaging. *Analyst* **2010**, *135*, 3220−3226.
(85) Szekeres, G. P.; Kneipp, J. SERS Probing of Proteins in Gold Nanoparticle Agglomerates. *Front. Chem.* **2019**, *7*, 30.

https://doi.org/10.1021/acs.chemmater.4c00564
Chem. Mater. 2024, 36, 5192−5203